Development of a two-degree-of-freedom vibration generator for fabricating optical microstructure arrays

HANHENG DU,[1] WAISZE YIP,[1] ZHIWEI ZHU,[2] AND SANDY TO[1,*]

[1]*State Key Laboratory of Ultra-precision Machining Technology, Department of Industrial and Systems Engineering, The Hong Kong Polytechnic University, Kowloon, 999077, Hong Kong*
[2] *School of Mechanical Engineering, Nanjing University of Science and Technology, Nanjing, 210094, China*
[*]*sandy.to@polyu.edu.hk*

Abstract: Optical microstructure arrays on metallic surfaces are drawing ever-increasing attention due to the increasing requirements in optical systems. Although vibration generators are developed for generating optical microarrays with the ultra-precision diamond cutting process, the systematic research works on its mechanical design, working performance simulation, and numerical simulation of microstructure arrays has received less attention. In this study, a novel two-degree-of-freedom vibration generator (2DOF-VG) is designed based on the triangular amplification mechanism. To precisely simulate the working performance of this designed 2DOF-VG, the detailed multi-physics finite element method is proposed. Considering the three-dimensional geometric shape of the cutting tool, the cutting motion trajectory, and the elastic recovery of the workpiece material, the numerical simulation algorithm of the microstructure arrays generation is then established and used to precisely predict the surface topography of microstructure arrays. Finally, two types of unique microstructure arrays are fabricated, which demonstrates the feasibility and flexibility of the 2DOF-VG.

1. Introduction

Recently, with the fast development of optical systems for multi-function integration, optical microstructure arrays have received more and more attention due to their superior performance [1,2]. For example, micro-lens arrays, micro-grating arrays, compound eye structures, and retroreflective arrays are widely applied in imaging [3], light beam control [4], digital camera [5], and sensing [6]. But how to fabricate these microstructure arrays with high efficiency and low cost has acted as the research focus in both academic and engineering circles. To satisfy practical needs, several fabrication technologies have fastly been developed. According to the working principle of material removal, they can be classified into chemical [7,8], physical [9], and mechanical [10]. In general, chemical and physical processes, such as femtosecond laser and chemical wet etching, are often limited to particular materials and laborious multi-step processes with high costs. Besides, it is also difficult for the chemical and physical processes to get high-quality arrays.

Mechanical machining, such as diamond milling and ultra-precision diamond turning, is more deterministic and universal. In diamond milling, a ball milling tool is fixed to the high-speed spindle. And micro-optics arrays can be individually generated with the assistance of translational servo motions [11]. Micro-machining with the natural single-crystal diamond tools is well suited at this micro- to mesoscale [12]. Although no post-processing is required for the nanometric surface generation in micro-machining, its processing time is not acceptable for mass production.

To resolve the aforementioned problems, the vibration-assisted machining technique based on the cutting tool's tertiary vibration motion was proposed to fabricate the micro/nanostructure

arrays surface, which is widely considered to be a promising method for enhancing the machining efficiency and surface quality [13]. There are two main working principles for vibration generators: working in the resonant mode of the mechanical structure and working in the non-resonant mode of the mechanical structure. The resonant vibration generator works in the structural resonant frequency, normally more than 20kHz. Shamoto and Moriwaki [14] designed the ultrasonic resonant elliptical vibrator and applied it to fabricate micro grooving on the hardened steel. The vibrator has a structural resonant frequency of around 20kHz by exciting the two piezoelectric plates with the phase difference. Suzuki et al. [15] utilized the sandwiched mechanical structure to simultaneously generate large longitudinal and bending vibrations at 39kHz for machining of tungsten alloy, a kind of typical molding material in the optical industry. Inspiring by the development of the ultrasonic motor, Guo and Ehmann [16] designed a resonant mode two-degree-of-freedom vibration generator for texturing microstructures and the vibration frequency can be adjusted by changing the length of the end mass. Although the resonant mode generators could work in an ultrasonic frequency, they only operate at a fixed frequency and do not have active control over the tool motion trajectory, which limits the shape diversity of the fabricated microstructures and then influences the functionality of the microstructure arrays.

If the vibration trajectory of the cutting tool is actively controlled, there is only possible with a non-resonant vibration generator. In recent years, many attempts have shifted towards the design and analysis of the non-resonant vibration generator. To obtain a cutting tool motion with high bandwidth and large amplitude, Kim et al. [17] proposed a long-stroke vibration generator to fabricate the optical freefrom mirrors with a form accuracy of 0.15μm in peak-to-valley value error, but it only machines some simple microstructures since it has only one degree-of-freedom (DOF). Zhu et al. [18] designed the decoupled two-DOF flexural mechanism with a sort of Z-shaped flexure hinge and proposed the concept of the fast-tool-servo-assisted turning in the fabrication of micro-structured surfaces with scattering homogenization, but the working frequency of this device is below 200Hz. Lin et al. [19] designed two double parallel four-bar linkage mechanisms with the working frequency of up to 1197Hz and fabricated micro-dimple arrays on a planar face. However, these existing vibration generators usually suffer from low DOF and low bandwidth, which affects the machining flexibility and efficiency. Wang et al. [20] presented a two-DOF vibration generator based on the bridge-type amplification unit and proposed a general design guideline for the non-resonant vibration generator. The amplification unit adopts the bridge-type and the thickness of the thinnest part of this amplification unit was 0.2mm, which influences the output stiffness of the whole device.

To meet these current challenges in the development of the non-resonant vibration generators, this paper designs the quasi-ellipse amplification unit based on the triangular amplification mechanism to enhance the output stiffness of the whole device and simultaneously amplify the displacement of the piezoelectric actuators. Two amplification units are arranged into the orthogonal layout to provide two DOFs. To the best of our knowledge, there are very few attempts to simulate the working performance of the vibration generator by directly inputting the voltage signals into the piezoelectric actuator (PEA) and treat the mechanical structure and PEAs as an entire part. Most of the studies input the displacement or force signals into the vibration generator and ignore the roles of PEAs in the simulation. In addition, numerical simulation of the microstructure arrays generation can predict the surface topography of the microstructure arrays and provide the theoretical guidance in the selection of the process parameters before fabrication, but most of the current researches only consider the cutting edge and ignore the roles of rake face and clearance face of the cutting tool in fabricating. And several studies neglect the elastic recovery of the workpiece material in the numerical simulation, in which the elastic recovery plays a significant part in the microstructure arrays generation, especially soft metal, such as copper or aluminum alloy.

In this study, the objective is to develop a novel two-degree-of-freedom vibration generator (2DOF-VG) for fabricating the microstructure arrays on the metallic surface. Firstly, the quasi-ellipse amplification unit is proposed to solve the inherent drawback of the common bridge-type amplification unit and the mechanical design of the 2DOF-VG is introduced. Subsequently, the multi-physics finite element method is conducted to simulate its working performances, which considers the roles of PEAs and more truly simulates the working performances of the designed 2DOF-VG. In order to more precisely predict the microstructure arrays generation and provide the suitable process parameters before fabricating, a numerical simulation algorithm is presented by comprehensively considering the three-dimensional geometric shape of the cutting tool, cutting motion trajectory, and the elastic recovery of the workpiece material. Finally, the flexibility of the developed 2DOF-VG and the accuracy of the established numerical simulation algorithm are validated experimentally.

2. Mechanical design

The PEA is usually chosen to offer the input displacements, but it has the inherent disadvantage of only providing the small stroke. Therefore, its displacement is required to amplify by a mechanical structure for complying with the requirements of the microstructure arrays fabrication. The displacement amplification mechanism is generally categorized into a lever amplification and a triangular amplification [21], as shown in Fig. 1. For the lever amplification, the amplification ratio λ_l can be computed by analyzing the geometrical transform relationship of different links.

$$\lambda_l = \frac{d_2}{d_1} = \frac{l_2}{l_1} \tag{1}$$

where d_1 and d_2 are the input and output displacements, respectively; l_1 and l_2 are the lengths of different parts of the link in Fig. 1(a).

For the triangular amplification, the amplification ratio λ_t can be expressed:

$$\lambda_t = \frac{d_{BD}}{d_{AC}} = \lim_{\Delta\alpha\to0} \frac{\sin\alpha - \sin(\alpha - \Delta\alpha)}{\cos(\alpha - \Delta\alpha) - \cos\alpha} = \cot\alpha \tag{2}$$

where d_{AC} and d_{BD} are the input and output displacements, respectively; and α is the angle between the link and the horizontal line before the small geometric deformation, as shown in Fig. 1(b).

The lever amplification and triangular amplification have their own merits and drawbacks. For instance, the lever amplification usually has a larger amplification ratio but needs larger structural sizes. In general, the larger structural sizes lead to a lower working frequency. In comparison with the lever amplification, the triangular amplification has smaller structural sizes and a compact structure. In addition, its bilateral symmetric structure enables to minimize the undesired disturbance.

Based on the triangular amplification principle, in this study, the quasi-ellipse amplification unit (QEAU) is proposed to use by combining the ellipse-type with the rhombus-type. The QEAU has the advantages of efficient fabrication via the electrical discharge machining and fast assembly via the preload bolt. For realizing the two-dimensional motions in the machining plane, two QEAUs are arranged in an orthogonal layout to offer two independent motions since the orthogonal layout can decrease the coupling ratio by reducing the mutual influence of the two kinematic units. A flexure guidance unit (FGU) composed of two parallel leaf-spring flexure hinge is utilized to connect these two QEAUs.

The novel 2DOF-VG is developed and presented in Fig. 2(a). The periodic displacement motions offered by the PEA are firstly amplified by the QEAU, and consequently transferred to the cutting tool holder (CTH) by the FGU. The two preload bolts act as the preload spring to provide the constant force loads since the spring-load enhances the PEAs' dynamic push/pull
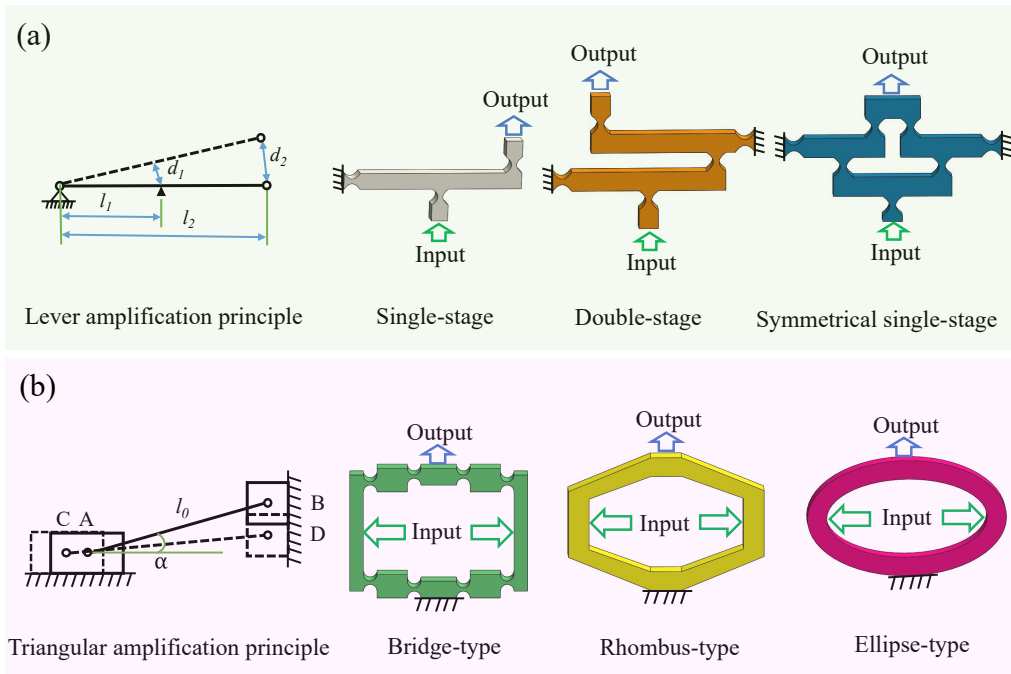
Fig. 1. The topology of two amplification mechanisms: a) lever amplification and b) triangular amplification.

performance. A natural single-crystal diamond cutting tool is fixed on the CTH, which is a commercially available triangular indexable insert. By independently actuating and amplifying the left and right PEAs, the two-dimensional periodic motions of the tool tip can be generated in the machining plane. The stainless steel 304 is selected as the main material due to its excellent corrosion resistance to various chemical corrodents. The monolithic 2DOF-VG was machined by the low-speed wire electrical discharge machining. The overall dimensions of this device are 51mm×32mm×5.9mm, as shown in Fig. 2(b). The main size l_2 and thickness w are decided by the length and width of the piezoelectric actuator. The length and width of the chosen piezoelectric actuator are 8 ± 0.1mm and 5.2 ± 0.1 mm, respectively. The values of l_2 and w are designed to be 8 mm and 5.9mm respectively for covering the whole piezoelectric actuator and avoiding the contact between other devices and the piezoelectric actuator during machining experiments. Then, other sizes, such as h_1 and l_1, are decided based on l_2 and w. The smaller sizes, the higher bandwidth. Therefore, other sizes are designed as small as possible. To compensate for manufacturing and assembly tolerance, the end plates are employed to fill the gap between the PEA and the QEAU. The main structural sizes and material properties of the 2DOF-VG are listed in Table 1 and Table 2 for providing the input parameters for the following simulation.

Table 1. Key sizes of the geometric structure of the 2DOF-VG

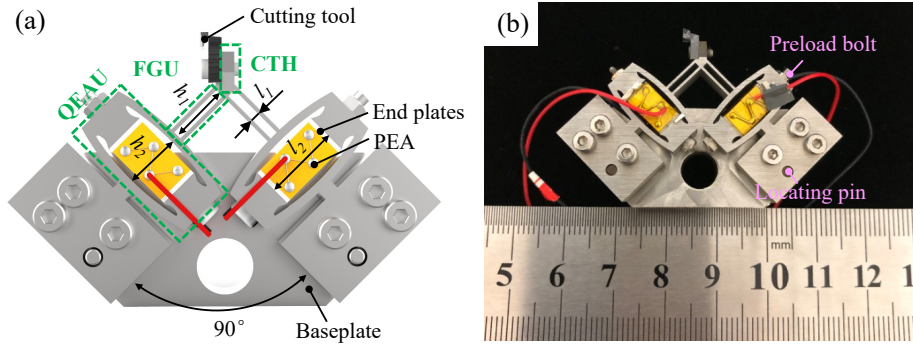| h_1	h_2	l_1	l_2	w
7.05mm	6.60mm	2mm	8mm	5.9mm

Fig. 2. The designed 2DOF-VG: (a) the 3D model and (b) the photograph.

Table 2. Material properties of the mechanical structure of the 2DOF-VG

Density	Young's modulus	Poisson's ratio	Shear modulus	Bulk modulus
7750 kg/m^3	1.93×10^{11} pa	0.31	7.37×10^{10} pa	1.70×10^{11} pa

3. Multi-physics simulation of the working performances

The accurate simulation of working performances can offer feedback guidance to optimize the mechanical structure and reduce the design time. The multi-physics finite element method (FEM) is utilized to precisely simulate and foretell the bandwidth and coupling ratio, which are the two significant quantitative indices of working performances. The bandwidth of the developed 2DOF-VG determines the range of usable working frequency, in which a higher working frequency means higher machining efficiency [20]. On the other hand, the coupling ratio influences the control of vibration trajectories, in which a lower coupling ratio means higher effectiveness on control during fabricating microstructure arrays [22].

3.1. Piezoelectric material property calculation

Determination of material properties is the first step in the multi-physics FEM process using the software ANSYS with Piezoelectric and MEMS extension. The piezoelectrical material properties include compliance matrix, stress piezoelectric coefficient matrix and the permittivity matrix at constant strain. According to electromechanical coupled constitutive relations of linear piezoelectricity, their relations are expressed as [23]:

$$\boldsymbol{S}_i = \boldsymbol{S}_{ij}^E \boldsymbol{T}_i + \boldsymbol{d}_{im} \boldsymbol{E}_m \tag{3}$$

$$\boldsymbol{D}_k = \boldsymbol{d}_{mi} \boldsymbol{T}_i + \boldsymbol{\varepsilon}_{mk}^T \boldsymbol{E}_k \tag{4}$$

$$\boldsymbol{T}_i = \boldsymbol{C}_{ij}^E \boldsymbol{S}_i - \boldsymbol{e}_{im} \boldsymbol{E}_m \tag{5}$$

$$\boldsymbol{D}_k = \boldsymbol{e}_{mi} \boldsymbol{S}_i + \boldsymbol{\varepsilon}_{mk}^S \boldsymbol{E}_k \tag{6}$$

where the vector $\boldsymbol{S}_i$ $\boldsymbol{T}_i$, $\boldsymbol{E}_{m/k}$ and $\boldsymbol{D}_k$ are the strain, stress, electric field, and electric displacement, respectively. The matrices $\boldsymbol{S}_{ij}^E$, $\boldsymbol{C}_{ij}^E$, $\boldsymbol{d}_{im/mi}$, $\boldsymbol{e}_{im/mi}$, $\varepsilon_{mk}^{T/S}$ are the mechanical compliance, the mechanical stiffness, the strain piezoelectric coefficient, the stress piezoelectric coefficient, and the permittivity, respectively. The subscript $i, j = 1, 2, \ldots, 6$ and $m, k = 1,2,3$ refer to different directions within the material coordinate system illustrated in Fig. 3. Axes 1, 2, and 3 correspond to the *x*-axis, *y*-axis, and *z*-axis, respectively while axes 4, 5, and 6 refer to rotational motion

around the x-axis, y-axis, and z-axis, respectively. The superscripts E, S, and T denote the measurements taken at the constant electric field, constant strain, and constant stress.

For the PEAs along the poling axis 3, the piezoelectric material is the transversely isotropic material. So several elements in the above matrices are either zero or expressed in terms of other parameters. Therefore, the fully constitutive Eq. (3) and Eq. (4) can be reduced as follow:

$$
\begin{bmatrix} S_1 \\ S_2 \\ S_3 \\ S_4 \\ S_5 \\ S_6 \end{bmatrix} =
\begin{bmatrix}
S_{11}^E & S_{12}^E & S_{13}^E & 0 & 0 & 0 \\
S_{12}^E & S_{11}^E & S_{13}^E & 0 & 0 & 0 \\
S_{13}^E & S_{13}^E & S_{33}^E & 0 & 0 & 0 \\
0 & 0 & 0 & S_{44}^E & 0 & 0 \\
0 & 0 & 0 & 0 & S_{55}^E & 0 \\
0 & 0 & 0 & 0 & 0 & S_{66}^E
\end{bmatrix}
\begin{bmatrix} T_1 \\ T_2 \\ T_3 \\ T_4 \\ T_5 \\ T_6 \end{bmatrix} +
\begin{bmatrix}
0 & 0 & d_{31} \\
0 & 0 & d_{31} \\
0 & 0 & d_{33} \\
0 & d_{15} & 0 \\
d_{15} & 0 & 0 \\
0 & 0 & 0
\end{bmatrix}
\begin{bmatrix} E_1 \\ E_2 \\ E_3 \end{bmatrix}
\tag{7}
$$

$$
\begin{bmatrix} D_1 \\ D_2 \\ D_3 \end{bmatrix} =
\begin{bmatrix}
0 & 0 & 0 & 0 & d_{15} & 0 \\
0 & 0 & 0 & d_{15} & 0 & 0 \\
d_{31} & d_{31} & d_{33} & 0 & 0 & 0
\end{bmatrix}
\begin{bmatrix} T_1 \\ T_2 \\ T_3 \\ T_4 \\ T_5 \\ T_6 \end{bmatrix} +
\begin{bmatrix}
\varepsilon_{11}^T & 0 & 0 \\
0 & \varepsilon_{22}^T & 0 \\
0 & 0 & \varepsilon_{33}^T
\end{bmatrix}
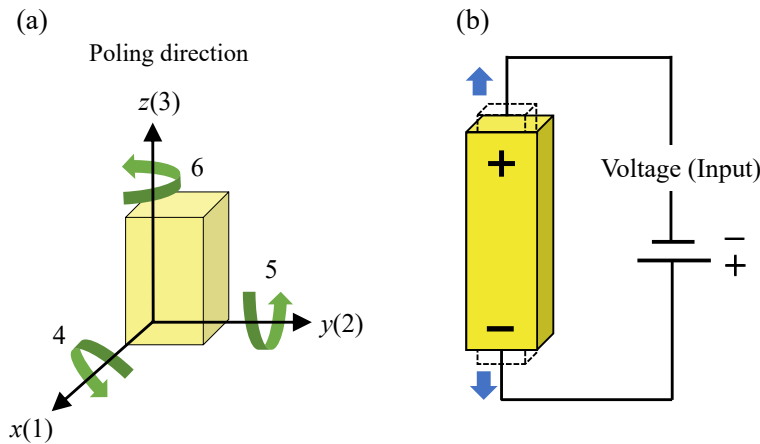\begin{bmatrix} E_1 \\ E_2 \\ E_3 \end{bmatrix}
\tag{8}
$$

Fig. 3. (a) The axis nomenclature in the piezoelectric material and (b) the schematic of the working principle of the PEA.

For the mechanical compliance matrix (S_{ij}^E), the elements S_{11}^E and S_{33}^E are usually obtained by the supplier of PEAs (Thorlabs, PK4FA2H3P2), as listed in Table 3. The other elements (S_{12}^E, S_{13}^E, S_{44}^E and S_{66}^E) in Eq. (7) can be obtained according to the computation method from [24]. Note that, in IEEE standard, the rows are defined as x, y, z, yz, xz, and xy, while multi-physics FEM input is expected to be ordered as x, y, z, xy, yz, and xz, so the conversion from IEEE format to ANSYS format is necessary accordingly.

Table 3. Piezoelectric material property provided by the supplier

Mechanical compliance coefficient (m²/N)	Strain piezoelectric coefficient (C/N)	Permittivity coefficient at constant stress
	$d_{31}=-320\times10^{-12}$	$\varepsilon_{11}^{T}=3370$
$S_{11}^{E}=17\times10^{-12}$	$d_{33}=4.67\times10^{-8}$	$\varepsilon_{22}^{T}=3370$
$S_{33}^{E}=23\times10^{-12}$	$d_{15}=950\times10^{-12}$	$\varepsilon_{33}^{T}=3300$

Then, the stress piezoelectric coefficient matrix $\boldsymbol{e}_{mi}$ and the permittivity matrix ε_{mk}^{S} at constant strain can be derived from Eq. (3)–(6):

$$\boldsymbol{e}_{mi} = \boldsymbol{d}_{mi}[\boldsymbol{S}_{ij}^{E}]^{-1} \tag{9}$$

$$\boldsymbol{\varepsilon}_{mk}^{S} = \boldsymbol{\varepsilon}_{mk}^{T} - \boldsymbol{d}_{mi}[\boldsymbol{e}_{mi}]^{T} \tag{10}$$

where $[\boldsymbol{S}_{ij}^{E}]^{-1}$ is the inverse of the compliance matrix $\boldsymbol{S}_{ij}^{E}$ and $[\boldsymbol{e}_{mi}]^{T}$ is the transpose of the stress piezoelectric coefficient matrix $\boldsymbol{e}_{mi}$. Note that the element d_{33} in the Eq. (9) and Eq. (10) presents all stacks' the strain piezoelectric coefficient along the poling direction.

3.2. Simulation process

Apart from the material properties of PEA, the material properties of mechanical structure such as density, Young's modulus, and Poisson's ratio, are required to set into the same as the actual situation. For the input of the boundary conditions in the multi-physics FEM, the baseplate is fixed to constrain all degrees of freedom, as shown in Fig. 4.
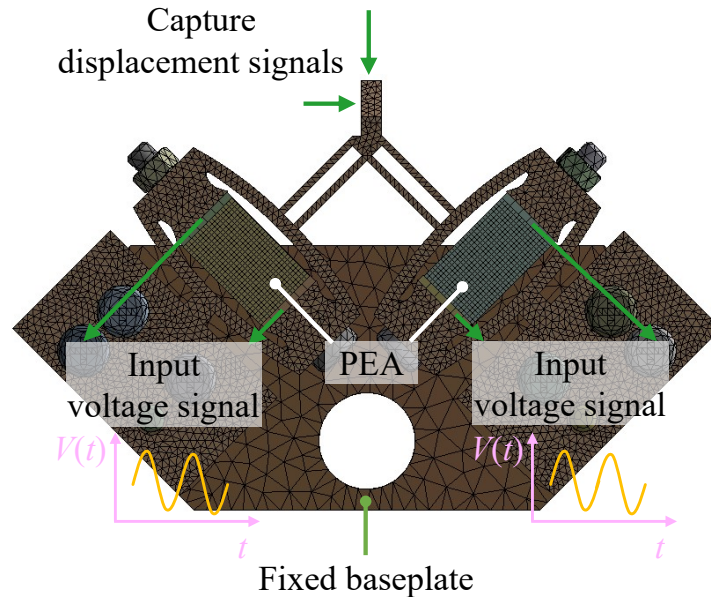
Fig. 4. Meshed multi-physics FEM model of the 2DOF-VG.

The swept method was performed to exam the bandwidth of the designed 2DOF-VG. The amplitude of sinusoidal voltage signals inputted into the left and right PEAs was 5 V with the 0° phase difference between the two signals. And the frequency linearly increased from 0 to 4000

Hz with a step size of 10Hz. The corresponding amplitudes of the output displacement were extracted for analyses of the bandwidth.

Most of the symmetric mechanisms have a strong coupling effect that causes undesirable parasitic motions, which add difficulty to the positioning of the cutting tool and then influence the shape accuracy of the fabricated microstructures. The coupling ratio is widely regarded as the most essential index to demonstrate motion accuracy and control stability for the vibration generator [25]. In terms of the coupling ratio simulation, the two sinusoidal voltage signals with the identical amplitude of 30V and the identical frequency of 10 Hz were inputted into the left and right PEAs. The phase difference between the two PEAs was set to 0° for pure depth-of-cutting motion and 180° for pure cutting motion. The vibration displacements of the cutting tool holder can be captured and recorded to analyze the coupling ratio of the 2DOF-VG in this multi-physics FEM.

4. Numerical simulation of the microstructure arrays generation

Figure 5 demonstrates the principle of microstructure arrays generation. When the ultrafast vibration motions of the 2DOF-VG are applied to fabricate the microstructure arrays on metallic surfaces, the complex interactions between the cutting tool and the workpiece will occur [26]. During fabricating, the three-dimensional geometric shape of the cutting tool, cutting trajectory, and the effects of material elastic recovery determine the shapes and sizes of microstructures. For instance, the clearance angle of the cutting tool plays a key role in shaping the final surface topography of microstructures because of the interference between the clearance face and the machined surface. The spacing (*d*) of the adjacent microstructures can be determined by the working frequency of the 2DOF-VG and the cutting speed.
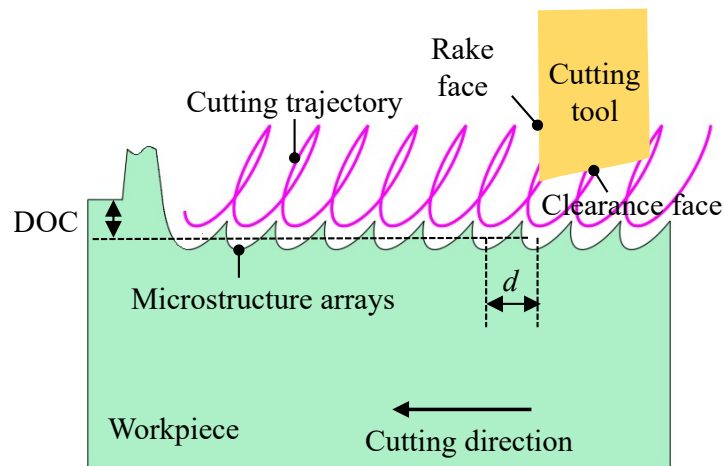

Fig. 5. Principle of microstructure arrays generation.

A numerical simulation algorithm of the microstructure arrays generation is proposed based on comprehensive consideration of the three-dimensional geometric shape of the cutting tool, the cutting motion trajectory, and the elastic recovery of workpiece material, which not only predicts the surface topography of microstructure arrays but also provides guidance in the selection of the process parameters before fabricating the desired microstructure arrays. The overall flowchart of this algorithm is illustrated in Fig. 6. The cutting tool geometry, including the rake face, clearance face, and cutting edge, is firstly discretized by the parametric functions. The workpiece geometry (a rectangle) is also discretized and stored in the form of mesh grids in the Cartesian coordinate system. The cutting tool coordinates with motion trajectories are the time-varying functions

$(t = N_i\Delta t)$, which are then transformed to the workpiece coordinate system through the coordinate transformation. Next, as the cutting tool intersects with the workpiece, the interference condition will be checked according to the Z value difference between the motion trajectory coordinate and the corresponding workpiece discretization point (grid point). The Boolean operation will be conducted to update the Z value of the workpiece grid point, as shown in the green parts of Fig. 6. Then, the material elastic recovery of the workpiece will be evaluated to predict the three-dimensional microstructures accurately. The Z value of the workpiece grid point will be further updated considering the material recovery. When completing cutting motion in the X-axis, the cutting tool returns to the origin point in the X-axis and feed along the Y-axis, as shown in the coffee color parts of Fig. 6. Finally, the surface topography of the microstructure arrays can be plotted through the programming of Matlab.
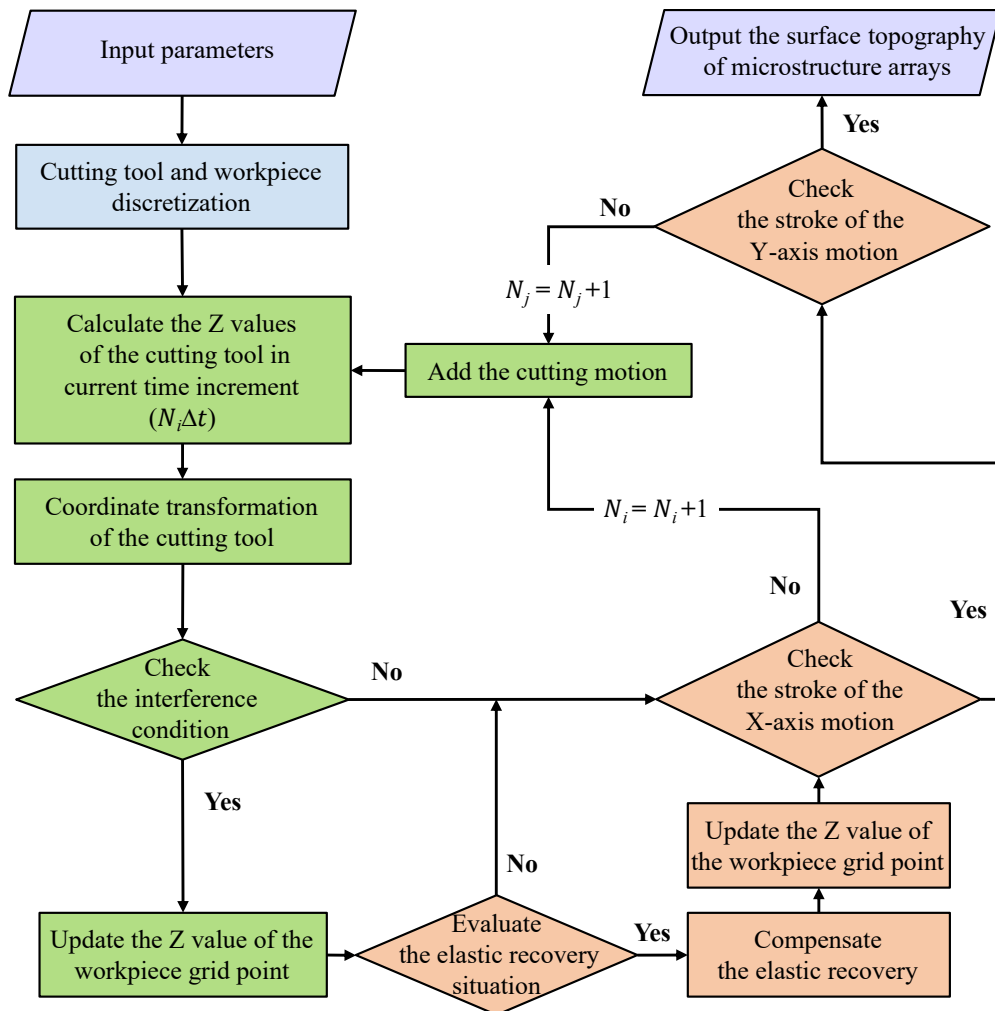

Fig. 6. Flowchart of the numerical simulation algorithm.

4.1. Discretization of the cutting tool and workpiece

A standard equilateral triangular insert with an internal angle of 60° is employed as the cutting tool, which scanning electron microscope (SEM) images are shown in Fig. 7. The cutting edge can be defined as an intersection between the rake face and the clearance face. In micro-machining, the cutting depth is far smaller than the nose radius of the cutting tool, so only small parts of the cutting tool need to be discretized. According to [26], the three-dimensional geometric shape of the cutting tool can be mathematically described in the local coordinate system by a set of parametric functions:

$$
\begin{aligned}
x_{insert}(m, n) &= \begin{cases} -(R + m)\sin n & m \le 0 \\ -(R - m\sin\alpha)\sin n & m > 0 \end{cases} \\
y_{insert}(m, n) &= \begin{cases} 0 & m \le 0 \\ m\cos\alpha & m > 0 \end{cases} \\
z_{insert}(m, n) &= \begin{cases} (R + m)\cos n & m \le 0 \\ (R - m\sin\alpha)\sin n & m > 0 \end{cases}
\end{aligned}
\tag{11}
$$

where the parameter m is an indicator of the different parts of the cutting tool. When $m>0$, the segment function describes the clearance face, while it describes the rake face when $m<0$. The cutting edge is described when $m=0$. n is the angle between the discretization point D and the tip E of the cutting tool, as shown in Fig. 8(a). R is the radius of the tool nose.
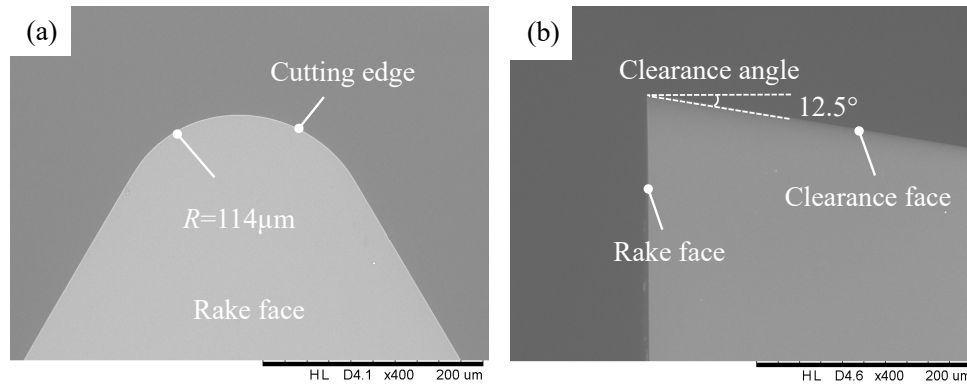

Fig. 7. SEM images of the cutting tool: (a) top view and (b) side view.

For the workpiece, its geometric shape is a rectangle in the microstructure arrays fabrication. The discretization result in the orthogonal coordinate system is shown in Fig. 8(b).

4.2. Modelling of the cutting motion trajectory

Before expressing the cutting motion trajectory, two three-dimensional Cartesian coordinate systems need to be defined, as depicted in Fig. 8(a) and 8(b). The cutting tool coordinate system $(o_t\text{-}x_ty_tz_t)$ is attached on the rake face of the cutting tool. And the three-dimensional shape of the cutting tool is described mathematically in this coordinate system. The workpiece coordinate system $(o_w\text{-}x_wy_wz_w)$ is established on the workpiece surface. Considering the vibration trajectory (D_t) of the cutting tool, the discretization coordinates (C_d) of the cutting tool, and the cutting
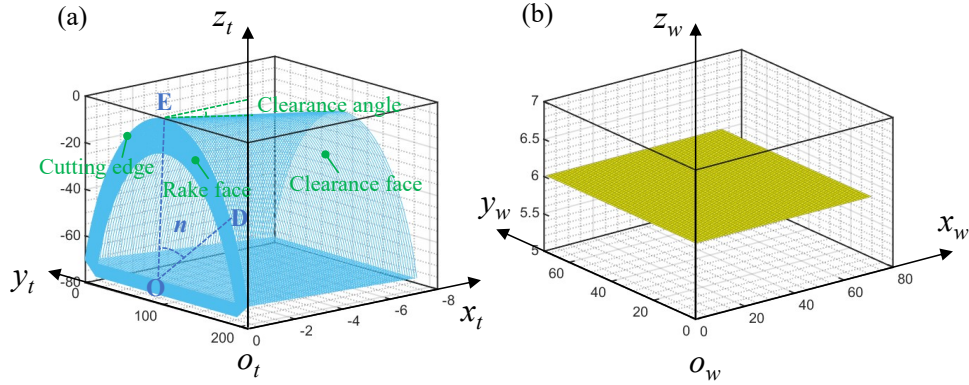
Fig. 8. Discretization results of (a) the cutting tool and (b) the workpiece.

speed (V_c) in the o_t-$x_t y_t z_t$ coordinate system, the motion trajectory coordinate (M_w) of the cutting tool in the o_w-$x_w y_w z_w$ coordinate system can be mathematically expressed as:

$$M_w = \mathbf{R}(\theta)\mathbf{T}(W_l - V_c N_i \Delta t, V_f N_j, \text{DOC})(C_d + D_t) \tag{12}$$

where $\mathbf{R}$ and $\mathbf{T}$ are the rotation and translation matrices [26], which let the tool tip motion in the local coordinate system transform into the workpiece coordinate system; θ is the rotation angle between the o_t-$x_t y_t z_t$ coordinate system and the o_w-$x_w y_w z_w$ coordinate system, and it equals zero as there is no rotation angle in these two coordinate systems; W_l is the length of the workpiece, i.e. the stroke of the X-axis motion; N_i is an increment and it increases by 1 on each iteration; Δt is the time step of the simulation, and Δt can be given by $min{1/V_c, 1/60f}$, in which f is the working frequency of the 2DOF-VG; V_f is the cross-feed along the Y-axis direction of the ultraprecision lathe; N_j is also an increment of the cycle number of cross-feed motion, and its value is determined by the ratio of the stroke of the Y-axis motion over the cross-feed.

The discretization coordinates C_d and vibration trajectory D_t of the cutting tool can be described by:

$$C_d = \begin{bmatrix} x_{insert}(m, n) \\ y_{insert}(m, n) \\ z_{insert}(m, n) \end{bmatrix} \tag{13}$$

$$D_t = \begin{bmatrix} D_t(x, N_i \Delta t) \\ D_t(y, N_i \Delta t) \\ D_t(z, N_i \Delta t) \end{bmatrix} \tag{14}$$

where $D_t(x, N_i \Delta t)$, $D_t(y, N_i \Delta t)$, and $D_t(z, N_i \Delta t)$ are the vibration trajectory components in the o_t-$x_t y_t z_t$ coordinate system.

Therefore, the motion trajectory coordinate of the cutting tool in the o_w-$x_w y_w z_w$ coordinate system can be written as:

$$
\begin{bmatrix} W_x \\ W_y \\ W_z \\ 1 \end{bmatrix} = \begin{bmatrix} \cos\theta & \sin\theta & 0 & 0 \\ -\sin\theta & \cos\theta & 0 & 0 \\ 0 & 0 & 1 & 0 \\ 0 & 0 & 0 & 1 \end{bmatrix} \begin{bmatrix} 1 & 0 & 0 & W_l - V_c N_i \Delta t \\ 0 & 1 & 0 & V_f N_j \\ 0 & 0 & 1 & DOC \\ 0 & 0 & 0 & 1 \end{bmatrix} \left\{ \begin{bmatrix} x_{insert}(m,n) \\ y_{insert}(m,n) \\ z_{insert}(m,n) \\ 1 \end{bmatrix} + \begin{bmatrix} D_t(x, N_i \Delta t) \\ D_t(y, N_i \Delta t) \\ D_t(z, N_i \Delta t) \\ 0 \end{bmatrix} \right\}
$$

$$
= \begin{bmatrix} 1 & 0 & 0 & W_l - V_c N_i \Delta t \\ 0 & 1 & 0 & V_f N_j \\ 0 & 0 & 1 & DOC \\ 0 & 0 & 0 & 1 \end{bmatrix} \left\{ \begin{bmatrix} x_{insert}(m,n) \\ y_{insert}(m,n) \\ z_{insert}(m,n) \\ 1 \end{bmatrix} + \begin{bmatrix} D_t(x, N_i \Delta t) \\ D_t(y, N_i \Delta t) \\ D_t(z, N_i \Delta t) \\ 0 \end{bmatrix} \right\}
$$

(15)

For each iteration, if the Z value of the motion trajectory coordinate is less than the Z value of the workpiece gird point, which means that the cutting tool intersects with the workpiece, the Z value of the corresponding workpiece gird point is replaced by the Z value of the motion trajectory coordinate. The Z value of the workpiece grid point is updated for the first time.

4.3. Evaluation of the material elastic recovery

As the chosen workpiece material is generally soft metal such as copper alloy or aluminum alloy, the elastic recovery related to cutting thickness must be considered in the numerical simulation algorithm. Zhu et al. [27] illustrated the material elastic recovery between the cutting tool and the workpiece during the diamond micromachining processing, as shown in Fig. 9(a). In this study, a piecewise function is used to express the elastic recovery concerning cutting thickness (t_c), as shown in Fig. 9(b). When t_c is smaller than the elastic deformation limit (t_e), which is taken as 0.01μm [26], the material is considered to experience a full recovery with no plastic deformation. The microstructure arrays fabrication process turns into a pure sliding process. When t_c is between the t_e and the minimum chip thickness (h_{min}), part of the material elastically recovers. The fabrication process turns into a ploughing process. When t_c increases over the h_{min}, only the elastic recovery occurs. The elastic recovery remains a constant value, and the shear process plays the main role in this process. The piecewise function of the material elastic recovery can be mathematically given as:

$$
\delta t_c = \begin{cases} t_c & t_c < t_e \\ \frac{(1-\varepsilon_p)h_{min}-t_e}{h_{min}-t_e}(t_c - t_e) & t_c \in [t_e, h_{min}] \\ t_e & t_c > h_{min} \end{cases}
$$

(16)

where ε_p is the plastic strain [27].

The Z value of the workpiece grid point is updated again according to the value of the material elastic recovery. Finally, the results of the numerical simulation algorithm of the microstructure arrays generation can be shown through the programming of Matlab.
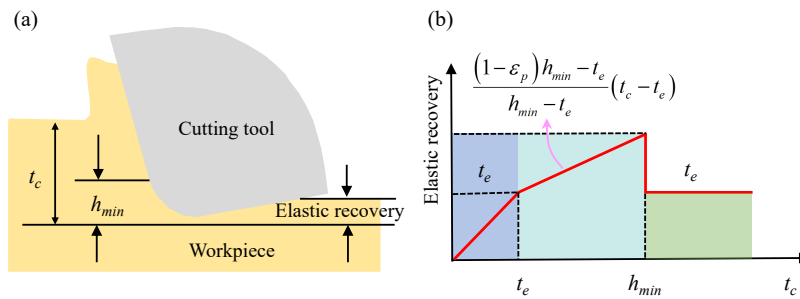
Fig. 9. (a) The illustration of material elastic recovery and (b) the elastic recovery function with respect to cutting thickness.

5. Experimental details

5.1. Working performance test

For verifying the effectiveness of the established multi-physics FEM, a test platform for working performances was established and shown in Fig. 10(a). In this platform, the computer offers the digital signals using a graphical programming software "LabVIEW". The digital signals would be converted and amplified by the multifunction I/O device (NI DAQ USB-6341) and the high-performance piezo amplifier (PI, E-617.001) to drive the PEAs. The displacement signals of the cutting tool holder along the cutting direction and DOC direction, as shown in Fig. 10(b), can be precisely measured by a pair of capacitive displacement sensors (Elite, Lion Precision). Besides, LabVIEW's user-interface has the capability of observing and monitoring the frequency response in real-time, which can help to adjust the time to stop the measure. To efficiently reduce the external disturbance, the testing experiments were carried out on a commercial platform with air-bearing supports.
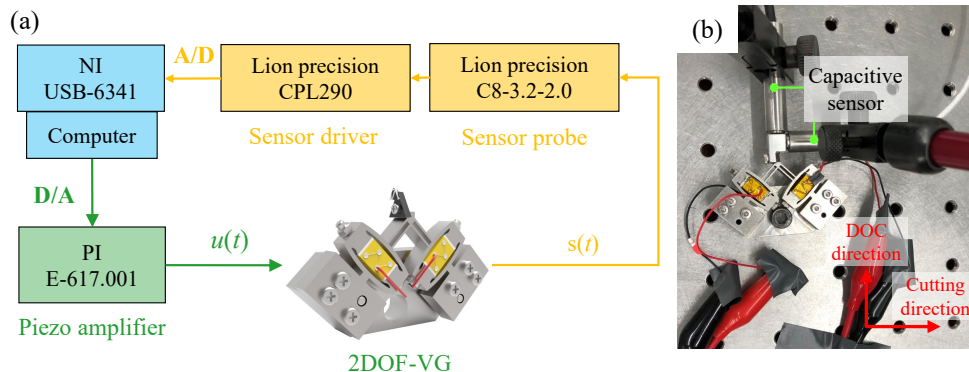

Fig. 10. The working performance test platform of the 2DOF-VG: (a) the schematic diagram and (b) the hardware platform.

The bandwidth and coupling ratio of the designed 2DOF-VG were tested and the voltage signals inputted into PEAs kept the same as the multi-physics FEM.

5.2. Microstructure arrays fabrication

The fabrication of microstructure arrays with the designed 2DOF-VG does not only demonstrate the capability of the device in fabricating different microstructure arrays but also verifies the

effectiveness and accuracy of the proposed numerical simulation algorithm of the microstructure arrays generation simultaneously. They were performed on a four-axis ultraprecision lathe (Moore Nanotech 350FG) with three linear axes and an air bearing spindle. The developed 2DOF-VG was fixed on the micro height adjust tool holder and the workpiece (the copper alloy H62, Keple Technology Co., Ltd, China) was fixed on a fixture that mounted on the spindle through the vacuum chuck. The properties of H62 are listed in Table 4.The single-crystal diamond cutting tool (Contour Fine Tooling Inc., UK) with a round edge was selected for fabricating the microstructure arrays. Its nose radius, clearance angle, and rake face angle are 0.114mm, 12.5°, and 0°, respectively. The workpieces were firstly flatted with a spindle speed of 2000rpm, and the nominal DOC and feedrate were set as 2μm and 2mm/min, respectively. The detailed hardware setup is shown in Fig. 11.
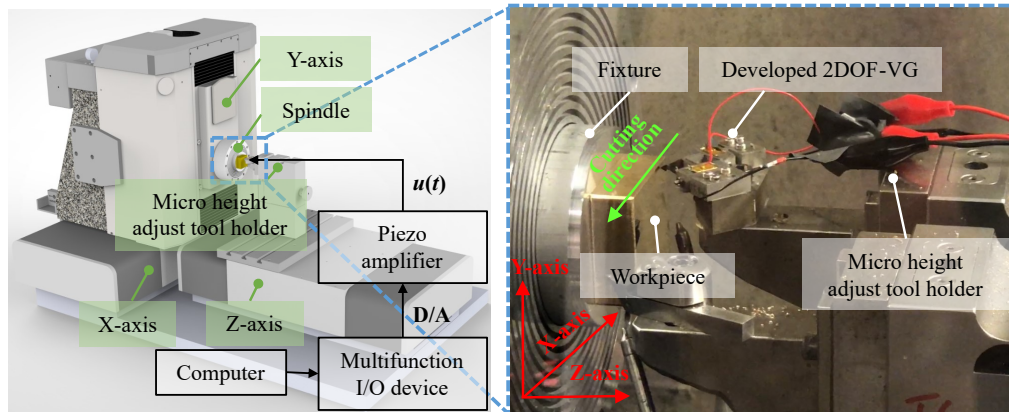

Fig. 11. The experimental setup for fabricating microstructure arrays.

Table 4. The properties of the copper alloy H62

Chemical composition (Weight, %)				Mechanical properties	
Cu	60.5–63.5	Sb	≤0.005	Density (Kg/m³)	8430
Fe	≤0.15	Bi	≤0.002	Elongation (%)	32.6
Pb	≤0.08	Zn	Balance	Tensile strength (Mpa)	392
P	≤0.01	Impurity	≤0.5	Hardness (Hv)	121

To compare the experimental results with the numerical simulation results, two samples were fabricated with unique microstructure arrays. They were named as two cases in this article. The detailed process parameters for the two cases are tabulated in Table 5. The sinusoidal voltage signals were applied in all experiments. The input parameters for the numerical simulation algorithm were kept the same as the fabrication experiments. After experiments, the workpieces were cleaned in the ultrasonic cleaner using the alcohol for 10 minutes to wash off any residual chips and then dried in an air environment for 20 minutes. A white light interferometer with sub-nanometre resolution (Zygo Nexview) was employed to characterize the three-dimensional surface topography of the microstructure arrays.

Table 5. The process parameters

	Parameters	Case 1	Case 2
	Depth-of-cutting	2μm	4μm
Cutting parameters	Cutting velocity	1000mm/min	600mm/min
	Cross-feed	60μm	30μm
	Amplitude	40V	40V
Voltage signal parameters	Frequency	500Hz	1000Hz
	Phase difference	30°	30°

6.　Results and discussion

6.1.　Working performances

In terms of the bandwidth, the results of the simulation and the measurement about the amplitudes of vibration displacements along the DOC direction are shown in Fig. 12. It can be clearly seen that the values of the first-order resonant frequency for the traditional simulation, the multi-physics FEM simulation, and measurement are 3330Hz, 3280Hz, and 3230Hz, respectively. The deviation (1.5%) of the multi-physics FEM simulation method is smaller than that (3.1%) of the traditional simulation method that simply inputs the displacement signals into the vibration generator. The amplitudes are stable and keep at 0.12μm before 3000Hz, so the bandwidth of the whole 2DOF-VG can be determined as to 3kHz. This means the usable working frequency of the developed 2DOF-VG ranges from 0Hz to 3kHz. Besides, although the first-order resonant frequency from the multi-physics FEM simulation result is a little larger than that of the measurement result as no damping controls are set in the simulation, the overall trend of this simulation method and the measurement is well in accordance with each other.
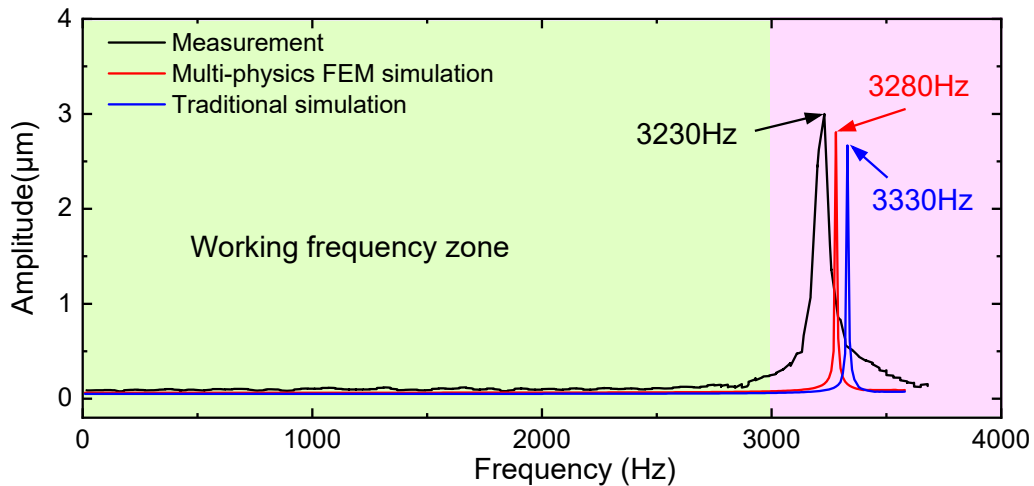

Fig. 12. Measurement and simulation results of the bandwidth.

As for the coupling ratio of the designed 2DOF-VG, the simulated displacement trajectories along DOC direction and cutting direction were captured in multi-physics FEM simulation, as shown in Fig. 13(a). The measurement and simulation results about coupling ratio are plotted in Figs. 13(b) and 13(c) respectively. The amplitudes of the traditional simulation, the multi-physics FEM simulation and the measurement are 1.90μm, 2.38μm, and 2.59μm in cutting direction. The smaller discrepancy show that multi-physics FEM can be a very effective tool for analyzing the

coupling ratio. According to the amplitude diversity between the desired motion and parasitic motion in the measurement results, the coupling ratios in the cutting direction and the DOC direction can be calculated as 2.32% and 4.86%, respectively.
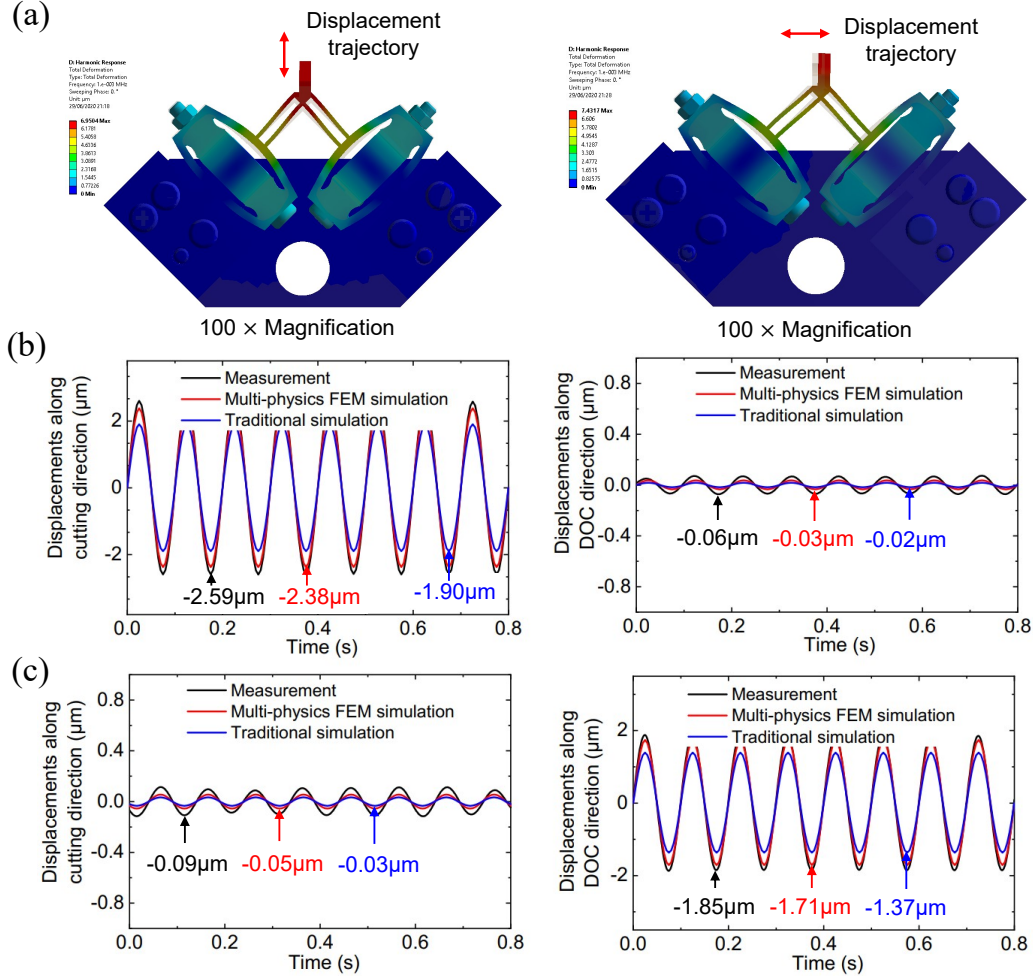

Fig. 13. Measurement and simulation results of the coupling ratio: (a) simulated displacement trajectories; displacements (b) along the cutting direction and (c) along the DOC direction.

In addition, the relationship between the input voltage signal and the output vibration trajectory can be expressed as:

$$
\begin{bmatrix} D_d \\ D_c \end{bmatrix} = \begin{bmatrix} A_d & A_d \\ A_c & -A_c \end{bmatrix} \begin{bmatrix} V_{left}(t) + V_{left}^0 \\ V_{right}(t) + V_{right}^0 \end{bmatrix}
\tag{17}
$$

where D_d and D_c are the vibration trajectory along DOC direction and cutting direction, respectively. $V_{left}(t)$ and $V_{right}(t)$ are the input voltage signal for the left PEA and right PEA, respectively. A_d and A_c are the transformation coefficients. V_{left}^0 and V_{right}^0 are the voltage offset for guaranteeing that resultant input voltages are always positive according to the working requirements of the PEAs.

According to the amplitudes of the input voltage signal and the output displacement in the experiments, the coefficients A_d (0.043μm/V) and A_c (0.031μm/V) can be calculated, which support to determine the input voltage signals of the PEAs according to the desired output displacement before fabricating.

6.2. *Microstructure arrays*

The surface topography of the microstructure arrays of the Case 1 and Case 2 are obtained after experiments and are shown in Figs. 14(a) and 14(b). It can be obviously found that the simulation results obtained by the proposed numerical simulation algorithm match well with the experiment results regarding both the shapes or sizes of the microstructure arrays on the metallic surface. In order to quantitatively analyze the geometrical errors between the experiment and the numerical simulation algorithm, the cross-sectional profiles are extracted, as shown in Fig. 14. For Case 1, the average value of the geometrical errors along the A-A cross-sectional profile is 0.1μm. For Case 2, the average value along the B-B cross-sectional profile is 0.02μm. These small geometrical errors validate the effectiveness and accuracy of this algorithm. Therefore, this algorithm is reliable to accurately predict the surface topography of the microstructure arrays and supports the process parameter selection before producing the desired microstructure arrays.
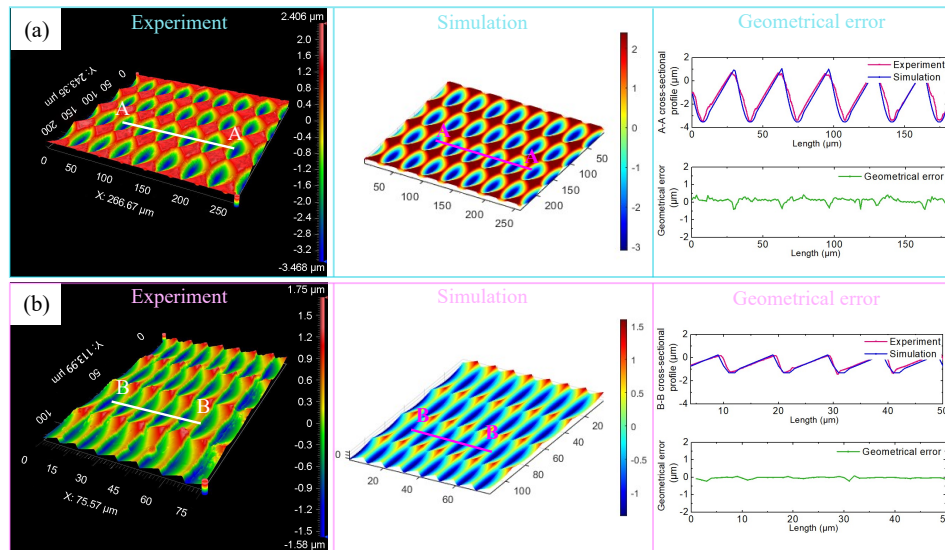

Fig. 14. Surface topography of the microstructure arrays and geometrical errors of (a) Case 1 and (b) Case 2.

In Case 1, the cutting velocity along the X-axis of the ultraprecision lathe was 1000mm/min and the DOC was 2μm. For the sinusoidal voltage signals that drove 2DOF-VG to generate the vibration trajectory, the amplitude, frequency, and phase difference between the two PEAs, were set as 40V, 500Hz, and 30°, respectively. When completing one cutting motion along X-axis, the cutting tool returned to the initial point in the X-axis and then fed 60μm along Y-axis. Finally, the micro-dimple arrays were machined on the copper alloy surface, as shown in Fig. 14(a). Similarly, the micro-ratchet arrays were generated for Case 2, as shown in Fig. 14(b).

Since both the cutting speed V_c and the working frequency f changes from Case 1 to Case 2, the spacing d along the cutting direction can be analyzed according to $d = V_c/f$. The experiment results about the spacing d decreases from 32.3μm in Case 1 to 9.9μm in Case 2, which agrees well with the theoretical analysis results (from 33.33μm to 10μm). Besides, in Case 2, the

significant decrease in the spacing *d* leads to serious interferences between the clearance face and machined surface, but the proposed numerical simulation algorithm enables to accurately predict the surface topography of the microstructure arrays, as shown in Fig. 14(b), which further demonstrates the flexibility and accuracy of this simulation algorithm.

Furthermore, no burr is observed at the boundaries of microstructure arrays, showing an evidence of better surface quality. To quantitatively evaluate the surface quality of fabricated microstructure arrays, three square areas (8μm ×8μm) are chosen from different regions for measuring the surface roughness (R_a) by using the atomic force microscopy technique. The measured average values of R_a are 7.52nm and 7.84nm for Case 1 and Case 2, respectively. The results indicate that a better surface finish can be achieved with the designed 2DOF-VG. Therefore, this designed 2DOF-VG can contribute to the successful industrial application of microstructure arrays fabrication.

7. Conclusions

In this study, a novel two-degree-of-freedom vibration generator (2DOF-VG) was developed for fabricating the two types of microstructure arrays on the metallic surface. The multi-physics finite element simulation of working performances, the numerical simulation algorithm of the microstructure arrays generation, and the verification experiments were systematically conducted to analyze, simulate, and verify the designed 2DOF-VG. The key conclusions are drawn as follows:

(1) The 2DOF-VG is developed based on the proposed quasi-ellipse amplification unit. And this 2DOF-VG has the capability to work at a frequency up to 3 kHz with a much lower coupling ratio (2.32% in the cutting direction and 4.86% in DOC direction).

(2) The multi-physics FEM is proposed in detail to simulate the working performances of the 2DOF-VG. The simulation results of the bandwidth and the coupling ratio (two quantitative indices of the working performances) are in good accordance with the measurement results, proving the effectiveness of this multi-physics FEM.

(3) The proposed numerical simulation algorithm precisely captures the surface topography of the microstructure arrays as the average geometrical error of this algorithm is less than 0.1μm, indicating that this algorithm enables to guide the process parameters selection before fabricating the desired microstructure arrays.

(4) The efficacy of the developed 2DOF-VG is demonstrated by the generation of micro-dimple arrays and micro-ratchet arrays with the average value of surface roughness (R_a) of less than 8nm, showing a better surface quality. These microstructure arrays make potential applications in industrial and engineering fields, especially in the optics area.

Disclosures. The authors declare no conflicts of interest.

Data availability. Data underlying the results presented in this paper are not publicly available at this time but may be obtained from the authors upon reasonable request.

References

1. H. Zuo, D.-Y. Choi, X. Gai, B. Luther-Davies, and B. Zhang, "CMOS compatible fabrication of micro, nano convex silicon lens arrays by conformal chemical vapor deposition," Opt. Express **25**(4), 3069 (2017).
2. C. Deng, H. Kim, and H. Ki, "Fabrication of a compound infrared microlens array with ultrashort focal length using femtosecond laser-assisted wet etching and dual-beam pulsed laser deposition," Opt. Express **27**(20), 28679 (2019).
3. T. Hou, C. Zheng, S. Bai, Q. Ma, D. Bridges, A. Hu, and W. W. Duley, "Fabrication, characterization, and applications of microlenses," Appl. Opt. **54**(24), 7366 (2015).

4. J. F. Algorri, P. Morawiak, D. C. Zografopoulos, N. Bennis, A. Spadlo, L. Rodríguez-Cobo, L. R. Jaroszewicz, J. M. Sánchez-Pena, and J. M. López-Higuera, "Multifunctional light beam control device by stimuli-responsive liquid crystal micro-grating structures," Sci. Rep. **10**(1), 1–10 (2020).

5. Y. M. Song, Y. Xie, V. Malyarchuk, J. Xiao, I. Jung, K. J. Choi, Z. Liu, H. Park, C. Lu, R. H. Kim, R. Li, K. B. Crozier, Y. Huang, and J. A. Rogers, "Digital cameras with designs inspired by the arthropod eye," Nature **497**(7447), 95–99 (2013).

6. R. Ahmed, A. K. Yetisen, S. H. Yun, and H. Butt, "Color-selective holographic retroreflector array for sensing applications," Light: Sci. Appl. **6**(2), e16214 (2017).

7. K. Lee, W. Wagermaier, A. Masic, K. P. Kommareddy, M. Bennet, I. Manjubala, S. W. Lee, S. B. Park, H. Cölfen, and P. Fratzl, "Self-assembly of amorphous calcium carbonate microlens arrays," Nat. Commun. **3**(1), 725 (2012).

8. S. Tong, H. Bian, Q. Yang, F. Chen, Z. Deng, J. Si, and X. Hou, "Large-scale high quality glass microlens arrays fabricated by laser enhanced wet etching," Opt. Express **22**(23), 29283 (2014).

9. F. Chen, Z. Deng, Q. Yang, H. Bian, G. Du, J. Si, and X. Hou, "Rapid fabrication of a large-area close-packed quasi-periodic microlens array on BK7 glass," Opt. Lett. **39**(3), 606 (2014).

10. A. Y. Yi and L. Li, "Design and fabrication of a microlens array by use of a slow tool servo," Opt. Lett. **30**(13), 1707 (2005).

11. Z. Sun, S. To, and K. M. Yu, "One-step generation of hybrid micro-optics with high-frequency diffractive structures on infrared materials by ultra-precision side milling," Opt. Express **26**(21), 28161 (2018).

12. D. Dornfeld, S. Min, and Y. Takeuchi, "Recent advances in mechanical micromachining," CIRP Annals **55**(2), 745–768 (2006).

13. X. Liu, D. Wu, J. Zhang, X. Hu, and P. Cui, "Analysis of surface texturing in radial ultrasonic vibration-assisted turning," J. Mater. Process. Technol. **267**, 186–195 (2019).

14. E. Shamoto and T. Moriwaki, "Ultraprecision diamond cutting of hardened steel by applying elliptical vibration cutting," CIRP Annals **48**(1), 441–444 (1999).

15. N. Suzuki, M. Haritani, J. Yang, R. Hino, and E. Shamoto, "Elliptical vibration cutting of tungsten alloy molds for optical glass parts," CIRP Ann. - Manuf. Technol. (2007).

16. P. Guo and K. F. Ehmann, "Development of a tertiary motion generator for elliptical vibration texturing," Precis. Eng. **37**(2), 364–371 (2013).

17. H. S. Kim, K. Il Lee, K. M. Lee, and Y. B. Bang, "Fabrication of free-form surfaces using a long-stroke fast tool servo and corrective figuring with on-machine measurement," Int. J. Mach. Tools Manuf. **49**(12-13), 991–997 (2009).

18. Z. Zhu, X. Zhou, Z. Liu, R. Wang, and L. Zhu, "Development of a piezoelectrically actuated two-degree-of-freedom fast tool servo with decoupled motions for micro-/nanomachining," Precis. Eng. **38**(4), 809–820 (2014).

19. J. Lin, J. Han, M. Lu, B. Yu, and Y. Gu, "Design, analysis and testing of a new piezoelectric tool actuator for elliptical vibration turning," Smart Mater. Struct. **26**(8), 085008 (2017).

20. J. Wang, H. Du, S. Gao, Y. Yang, Z. Zhu, and P. Guo, "An ultrafast 2-D non-resonant cutting tool for texturing micro-structured surfaces," J. Manuf. Process. **48**, 86–97 (2019).

21. M. Ling, J. Cao, M. Zeng, J. Lin, and D. J. Inman, "Enhanced mathematical modeling of the displacement amplification ratio for piezoelectric compliant mechanisms," Smart Mater. Struct. **25**(7), 075022 (2016).

22. F. Wang, Z. Huo, C. Liang, B. Shi, Y. Tian, X. Zhao, and D. Zhang, "A Novel Actuator-Internal Micro/Nano Positioning Stage with an Arch-Shape Bridge-Type Amplifier," IEEE Trans. Ind. Electron. **66**(12), 9161–9172 (2019).

23. E. Elka, D. Elata, and H. Abramovich, "The electromechanical response of multilayered piezoelectric structures," J. Microelectromechanical Syst. **13**(2), 332–341 (2004).

24. R. Clement, J. L. Huang, Z. H. Sun, J. Z. Wang, and W. J. Zhang, "Motion and stress analysis of direct-driven compliant mechanisms with general-purpose finite element software," Int. J. Adv. Manuf. Technol. **65**(9-12), 1409–1421 (2013).

25. H. Tang and Y. Li, "Development and Active Disturbance Rejection Control of a Compliant Micro-/Nanopositioning Piezostage with Dual Mode," IEEE Trans. Ind. Electron. **61**(3), 1475–1492 (2014).

26. P. Guo and K. F. Ehmann, "An analysis of the surface generation mechanics of the elliptical vibration texturing process," Int. J. Mach. Tools Manuf. **64**, 85–95 (2013).

27. W. Le Zhu, F. Duan, X. Zhang, Z. Zhu, and B. F. Ju, "A new diamond machining approach for extendable fabrication of micro-freeform lens array," Int. J. Mach. Tools Manuf. **124**, 134–148 (2018).